

Cite this: *Inorg. Chem. Front.*, 2023, **10**, 3273

# A new 0D–2D CsPbBr<sub>3</sub>–Co<sub>3</sub>O<sub>4</sub> heterostructure photocatalyst with efficient charge separation for photocatalytic CO<sub>2</sub> reduction†

 Xin Zhong,<sup>‡a</sup> Xinmeng Liang,<sup>‡a</sup> Xinyu Lin,<sup>a</sup> Jin Wang,<sup>id</sup> \*<sup>a,b</sup>  
 Malik Zeeshan Shahid<sup>id</sup> \*<sup>a</sup> and Zhengquan Li<sup>id</sup> \*<sup>a,b</sup>

The effective spatial separation of photogenerated charge carriers is essential for realizing efficient CO<sub>2</sub> conversion. Herein, a new CsPbBr<sub>3</sub>–Co<sub>3</sub>O<sub>4</sub> heterostructure photocatalyst was rationally developed for photocatalytic CO<sub>2</sub> reduction. A facile synthetic strategy based on electrostatic interactions was utilized. The results revealed that the CsPbBr<sub>3</sub>–Co<sub>3</sub>O<sub>4</sub> hybrid exhibited a boosted evolution rate of 64.6 μmol g<sup>-1</sup> h<sup>-1</sup> (CO: 35.40 μmol g<sup>-1</sup> h<sup>-1</sup>; CH<sub>4</sub>: 29.2 μmol g<sup>-1</sup> h<sup>-1</sup>) with an electron consumption rate ( $R_{\text{electron}}$ ) of 304.4 μmol g<sup>-1</sup> h<sup>-1</sup>, surpassing pristine CsPbBr<sub>3</sub> or Co<sub>3</sub>O<sub>4</sub>. The high activity mainly arises from efficient charge separation and the directional transfer of electrons from CsPbBr<sub>3</sub> to Co<sub>3</sub>O<sub>4</sub> via an intimately coupled heterointerface. Notably, the surface features (derived from the unique morphology) expedited the CO<sub>2</sub> adsorption and accumulation of electrons at the Co<sub>3</sub>O<sub>4</sub> site which ultimately facilitated the conversion of CO<sub>2</sub> over the CsPbBr<sub>3</sub>–Co<sub>3</sub>O<sub>4</sub> composite. This approach provides a strategy to design and modulate highly active metal oxide and perovskite-based photocatalysts and presents great potential for constructing a heterointerface for CO<sub>2</sub> reduction.

Received 21st March 2023,  
Accepted 17th April 2023

DOI: 10.1039/d3qi00527e

rsc.li/frontiers-inorganic

## 1. Introduction

The daily consumption of fossil fuels results in the emission of CO<sub>2</sub>, causing universal environmental and energy issues.<sup>1–4</sup> Fixation of CO<sub>2</sub> into value-added products such as CO, CH<sub>4</sub>, HCOOH, CH<sub>3</sub>OH, *etc.* via solar-driven catalysis, also known as artificial photosynthesis, is a clean and sustainable solution.<sup>5–7</sup> However, it is challenging and suffers low conversion efficiency due to the high thermodynamic stability of CO<sub>2</sub> molecules and the need for multi-electron transfer.<sup>8,9</sup> Recently, instead of using single-component photocatalysts, research efforts have been diverted to designing their low-cost heterostructures. Many materials, such as C<sub>3</sub>N<sub>4</sub>,<sup>10,11</sup> ZrO<sub>2</sub>,<sup>12</sup> TiO<sub>2</sub>,<sup>13</sup> Ta<sub>2</sub>O<sub>5</sub>,<sup>14</sup> Nb<sub>2</sub>O<sub>5</sub>,<sup>15</sup> metal sulfides,<sup>16</sup> metal–organic frameworks,<sup>17</sup> metal complexes,<sup>7</sup> single-atom catalysts,<sup>18</sup>

MXenes,<sup>19</sup> conducting polymers,<sup>20</sup> metal halide perovskites,<sup>6,21</sup> *etc.*, have been reported aiming at activity enhancement via optimizing the light-harvesting and charge carrier kinetics. However, the search for a more effective candidate photocatalyst has not stopped.

Among numerous materials, all inorganic metal halide perovskites, particularly cesium lead-bromide perovskite quantum dots (CsPbBr<sub>3</sub> QDs), are extremely competitive photocatalysts for CO<sub>2</sub> reduction.<sup>1,6,22,23</sup> This is owing to their suitable energy band structure, small size, defect tolerance, and large carrier mobility as compared to other inorganic metal halide family members, *e.g.* CsPbCl<sub>3</sub> and CsPbI<sub>3</sub>.<sup>1,6,24–43</sup> However, pristine CsPbBr<sub>3</sub> QDs suffer from instability and rapid recombination of electron–hole (e<sup>-</sup>–h<sup>+</sup>) pairs, leading to low activity. To address this issue, Xu *et al.* first utilized the CsPbBr<sub>3</sub> QDs/graphene composite for the photocatalytic reduction of CO<sub>2</sub>.<sup>43</sup> After that, several efforts were devoted to enhance its performance. For instance, our group designed CsPbBr<sub>3</sub> QDs/Bi<sub>2</sub>WO<sub>6</sub><sup>38</sup> and CsPbBr<sub>3</sub> QDs coupled with covalent triazine frameworks,<sup>36</sup> and both exhibited enhanced charge separation and led to improved CO<sub>2</sub> photoreduction. But the produced gas was mainly CO and only a minimum of CH<sub>4</sub> was detected. This was possibly due to the lack of sufficient accumulation of reductive electrons at catalytic sites.

<sup>a</sup>Key Laboratory of the Ministry of Education for Advanced Catalysis Materials, Zhejiang Normal University, Jinhua, Zhejiang 321004, P. R. China.

E-mail: zqli@zjnu.edu.cn, zeeshan-nano@zjnu.edu.cn, wangjin@zjnu.edu.cn

<sup>b</sup>Zhejiang Institute of Optoelectronics, Zhejiang Normal University, Jinhua, Zhejiang 321004, P. R. China

†Electronic supplementary information (ESI) available. See DOI: <https://doi.org/10.1039/d3qi00527e>

‡These authors contributed equally.

So, we further our research to find some suitable materials which can form an intimately coupled interface with CsPbBr<sub>3</sub> QDs and enable efficient photocatalysis to generate both CO and CH<sub>4</sub>, thereby overcoming the intrinsic issues of CsPbBr<sub>3</sub> QDs.

We found that the transition metal oxide photocatalyst cobalt oxide (Co<sub>3</sub>O<sub>4</sub>) is an ideal non-precious catalyst for CO<sub>2</sub> reduction as it exhibits suitable band alignment, efficient charge-carrier flux capability, and chemical/thermodynamic stability.<sup>44–52</sup> However, the typical single component Co<sub>3</sub>O<sub>4</sub> may suffer limited preservation of reductive electrons as well as hindered spatial separation of e<sup>−</sup>–h<sup>+</sup> pairs. Multiple morphologies have been constructed to meet such limitations, such as nanorods,<sup>53</sup> ultrathin nanosheets,<sup>54</sup> nanofibers,<sup>55</sup> hollow dodecahedra,<sup>48</sup> porous structures,<sup>56</sup> and mesoporous two-dimensional (2D) hexagonal nanoplatelets (HPs) with various facets and catalytically active sites.<sup>45,57</sup> For example, Gao *et al.* first developed [112] facet-rich Co<sub>3</sub>O<sub>4</sub> HPs,<sup>52</sup> and then later on Zhu *et al.* constructed the Co<sub>3</sub>O<sub>4</sub>/g-C<sub>3</sub>N<sub>4</sub> (2D/2D) hybrid,<sup>57</sup> both intended to facilitate the separation of charge carriers for photocatalytic CO<sub>2</sub> conversion. Inspiringly, we intend to develop a high-performance Co<sub>3</sub>O<sub>4</sub> heterostructure catalyst by simultaneously promoting charge separation and preserving the reductive electrons. It is widely accepted that constructing a heterostructure is efficient for channelizing and accelerating the separation and transfer of e<sup>−</sup>–h<sup>+</sup> pairs *via* a strongly coupled interface developed through proper band alignment and work functions ( $\Phi$ ).<sup>47,58–61</sup> Therefore, constructing a hybrid between CsPbBr<sub>3</sub> QDs and Co<sub>3</sub>O<sub>4</sub> HPs probably can result in an improved photocatalytic performance toward CO<sub>2</sub> reduction. To the best of our knowledge, there is no report on the fabrication of CsPbBr<sub>3</sub> QDs on Co<sub>3</sub>O<sub>4</sub> HPs, and it is desirable to design and construct a new heterostructure based on CsPbBr<sub>3</sub> QDs and Co<sub>3</sub>O<sub>4</sub> HPs for CO<sub>2</sub> photoreduction.

Herein, a CsPbBr<sub>3</sub>–Co<sub>3</sub>O<sub>4</sub> heterojunction photocatalyst is developed *via* electrostatic self-assembly between Co<sub>3</sub>O<sub>4</sub> HPs and CsPbBr<sub>3</sub> QDs for photocatalytic CO<sub>2</sub> reduction. Investigations confirmed the successful formation of the CsPbBr<sub>3</sub>–Co<sub>3</sub>O<sub>4</sub> hybrid. Diverse physicochemical and optoelectronic characterization studies revealed that: (i) Co<sub>3</sub>O<sub>4</sub> HPs acted as a supporting matrix to collect electrons from CsPbBr<sub>3</sub>, rendering electron localization; (ii) the CsPbBr<sub>3</sub>–Co<sub>3</sub>O<sub>4</sub> hybrid exhibited compact heterointerfaces, facilitating robust charge separation with hampered e<sup>−</sup>–h<sup>+</sup> pair recombination; (iii) the Co<sub>3</sub>O<sub>4</sub> side offers numerous mesopores and catalytic sites, which facilitate the better capturing and activation of CO<sub>2</sub> molecules. Consequently, CsPbBr<sub>3</sub>–Co<sub>3</sub>O<sub>4</sub> showed improved activity for the generation of CO and CH<sub>4</sub>, with an evolving rate of 35.40 and 29.2 μmol g<sup>−1</sup> h<sup>−1</sup>, respectively, surpassing their pristine counterparts *i.e.*, CsPbBr<sub>3</sub> QDs and Co<sub>3</sub>O<sub>4</sub> HPs, as well as recent state-of-the-art photocatalysts (Table S1†). This work highlights the rational design of new metal halide perovskite-based photocatalysts and addresses the critical issues regarding charge carrier kinetics to realize efficient solar-driven CO<sub>2</sub> conversion.

## 2. Experimental section

### 2.1. Synthesis of CsPbBr<sub>3</sub> QDs

To obtain CsPbBr<sub>3</sub> QDs, the reported method was followed (see also in Fig. S1†).<sup>62</sup> Briefly, for the Cs-OA stock solution, 0.2 g of cesium carbonate (Cs<sub>2</sub>CO<sub>3</sub>), 10 mL of octadecene (ODE, C<sub>18</sub>H<sub>36</sub>), and 0.6 mL of oleic acid (OA, C<sub>18</sub>H<sub>34</sub>O<sub>2</sub>) were loaded into a three-necked round bottom flask. Under Ar flow, the temperature was increased to 120 °C and a clear light-yellow solution was obtained. The temperature was increased to 150 °C just before the hot injection. For the Pb stock solution, 0.1380 g of lead bromide (PbBr<sub>2</sub>) and 10 mL of ODE were added into a 50 mL three-necked round bottom flask, under Ar flow, the temperature was increased to 120 °C to get a white turbid liquid and maintained it for 30 min. Next, the temperature was further increased to 165 °C, and 1.5 mL OA and 1.1 mL OAm were added to the Pb stocks. When a yellow homogeneous solution was obtained, 0.8 mL of the Cs-stock solution was swiftly injected into it. After 5 s, the mixture was immediately cooled down using an ice-water bath. The original solution was directly centrifuged at 8000 rpm for 5 min and further washed with ethyl acetate and isopropanol to remove the organic residue. Finally, the CsPbBr<sub>3</sub> QDs collected and stored in *n*-hexane are added in an equal volume.

### 2.2. Preparation of Co<sub>3</sub>O<sub>4</sub> HPs

To obtain Co<sub>3</sub>O<sub>4</sub> HPs, the previously reported method was modified (see also in Fig. S2†).<sup>52</sup> Firstly, β-Co(OH)<sub>2</sub> precipitates were prepared. 0.2379 g (5 mmol) of cobalt chloride hexahydrate (CoCl<sub>2</sub>·6H<sub>2</sub>O), 1.6823 g (60 mmol) of cyclohexamethylenetetramine (urotropine), 180 mL of deionized water and 20 mL of ethanol were added into a beaker under stirring. The mixture was heated in an oil bath to 90 °C for 1 h to obtain a pink solution. After cooling it to an ambient temperature, it was centrifuged at 9000 rpm for 15 min to obtain a pink precipitate of β-Co(OH)<sub>2</sub>. Subsequently, 50 mL of deionized water and 50 mL of ethanol were added, and the β-Co(OH)<sub>2</sub> precipitate was redispersed by ultrasonication. The sample was collected by centrifuging at 9000 rpm for 15 min. This operation was repeated 3 times. The obtained precipitate was freeze-dried under vacuum for 6 hours. Finally, the precipitate was transferred into a cuboid crucible and put into a muffle furnace for calcination at 400 °C for 3 h to obtain a black powder of Co<sub>3</sub>O<sub>4</sub> HPs.

### 2.3. Synthesis of the CsPbBr<sub>3</sub>–Co<sub>3</sub>O<sub>4</sub> heterostructure

The CsPbBr<sub>3</sub>–Co<sub>3</sub>O<sub>4</sub> heterostructure was prepared using a solution-processed approach at room temperature. First, 0.5 mg of the Co<sub>3</sub>O<sub>4</sub> HP powder was dispersed into 250 μL of ethanol under uninterrupted stirring. Second, 400 μL (2 mg) of CsPbBr<sub>3</sub> QDs were dispersed into 5 mL of ethyl acetate. Third, the CsPbBr<sub>3</sub> QD solution was swiftly added into the solution of Co<sub>3</sub>O<sub>4</sub> HPs and mechanically stirred at room temperature in the dark for 30 min. Finally, the mixture was ultrasonicated for another 30 min under ambient conditions. The obtained solution was centrifuged at 8000 rpm for 5 min, and the precipitate

was vacuum dried overnight at 45 °C to obtain the CsPbBr<sub>3</sub>-Co<sub>3</sub>O<sub>4</sub> heterojunction. This synthesis was performed with an optimum mass ratio (Co<sub>3</sub>O<sub>4</sub> HPs: CsPbBr<sub>3</sub> QDs) *i.e.*, 1:4, and a similar method was followed to obtain various mass ratios such as 1:1, 1:2, 1:8, and 1:16. Step by step addition of Co<sub>3</sub>O<sub>4</sub> HPs and CsPbBr<sub>3</sub> QDs as well as the formation process of the CsPbBr<sub>3</sub>-Co<sub>3</sub>O<sub>4</sub> heterojunction are also picturized and described in Fig. S3.† The details of all materials and other characterization studies for physicochemical and optoelectronic properties are provided in the ESI.†

### 3. Results and discussion

#### 3.1. Illustration of the synthesis process and verification of the heterostructure formation

Firstly, CsPbBr<sub>3</sub> QDs (0D) was precisely prepared *via* a typical hot-injection method (Fig. S1†).<sup>62</sup> Subsequently, Co<sub>3</sub>O<sub>4</sub> HPs (2D) holding rich facets [112] were synthesized through the calcination of brucite-like cobalt hydroxide β-Co(OH)<sub>2</sub> precipitates (Fig. S2†).<sup>52</sup> Finally, to obtain a 0D/2D CsPbBr<sub>3</sub>-Co<sub>3</sub>O<sub>4</sub> heterojunction, their mixture at an optimum mass ratio 4:1 (CsPbBr<sub>3</sub> QDs: Co<sub>3</sub>O<sub>4</sub> HPs) was exclusively stirred in a solution of ethyl acetate and ethanol at room temperature (Scheme 1, see details in Fig. S3†). The tactic used here is based on the Coulomb electrostatic assembly which enables the incorporation of CsPbBr<sub>3</sub> QDs and Co<sub>3</sub>O<sub>4</sub> HPs. The zeta potentials of pristine CsPbBr<sub>3</sub> QDs and Co<sub>3</sub>O<sub>4</sub> HPs are 4.80 mV and -3.10 mV, respectively (Fig. S4†), which indicates oppositely charged surfaces encounter electrostatic attractions, resulting in the formation of CsPbBr<sub>3</sub>-Co<sub>3</sub>O<sub>4</sub>. Such a kind of electrostatic self-assembly would possess a strong heterointerface, beneficial for interfacial charge transfer.<sup>63</sup>

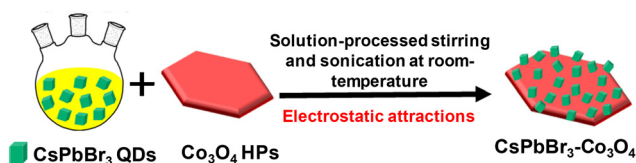
To confirm the successful formation of the CsPbBr<sub>3</sub>-Co<sub>3</sub>O<sub>4</sub> hybrid, powder X-ray diffraction (XRD) was first conducted (Fig. 1a). Pristine CsPbBr<sub>3</sub> QDs exhibit a typical cubic-phase (JCPDS card, No. 75-0412). Meanwhile, pristine Co<sub>3</sub>O<sub>4</sub> HPs show diffraction patterns associated with the face-centred cubic phase of the spinel Co<sub>3</sub>O<sub>4</sub> (JCPDS card No. 74-1657). Notably, strong signals of all peaks emerged and co-existed in the CsPbBr<sub>3</sub>-Co<sub>3</sub>O<sub>4</sub> hybrid, illustrating the successful formation of the heterojunction and the crystal phases were well maintained. To confirm this claim, nitrogen adsorption-desorption analysis was performed (Table S2†). It can be seen that after the precise formation of the heterojunction, the pore size and pore volume were reduced from 31.3 nm to 21.21 nm

and 0.1325 cm<sup>3</sup> g<sup>-1</sup> to 0.0266 cm<sup>3</sup> g<sup>-1</sup> respectively. In addition, the BET surface area also decreased from 16.9 m<sup>2</sup> g<sup>-1</sup> to 5.016 m<sup>2</sup> g<sup>-1</sup>. This result indicates that the mesopores of Co<sub>3</sub>O<sub>4</sub> were occupied by CsPbBr<sub>3</sub> QDs. Besides in the XRD, an exclusive color transformation was observed from black (Co<sub>3</sub>O<sub>4</sub>-HPs, Fig. 1b) and bright yellow (CsPbBr<sub>3</sub> QDs, Fig. 1c) to dark grey (CsPbBr<sub>3</sub>-Co<sub>3</sub>O<sub>4</sub>, Fig. 1d). In addition, under ultraviolet irradiation, the CsPbBr<sub>3</sub>-Co<sub>3</sub>O<sub>4</sub> heterojunction demonstrated a dark green fluorescence in comparison with the bright green fluorescence of CsPbBr<sub>3</sub> QDs (Fig. S5†). Such color transformations further endorse that the heterojunction was constructed successfully in a well-controlled manner *via* a current facile strategy.

Transmission electron microscopy (TEM) and scanning electron microscopy (SEM) analysis further confirmed the formation of the heterojunction. CsPbBr<sub>3</sub> QDs exhibited an average size of about 12 nm (Fig. 1e and inset), whereas Co<sub>3</sub>O<sub>4</sub> exhibits a hexagonal platelet-like structure with lateral sizes of ~4 ± 1 μm, and a thickness of about ~50 ± 10 nm, a dominant facet (112), and mesopores (Fig. 1f and inset). Importantly, after incorporating CsPbBr<sub>3</sub> QDs into Co<sub>3</sub>O<sub>4</sub> HPs, several facts were noticed. (i) Both CsPbBr<sub>3</sub> QDs and Co<sub>3</sub>O<sub>4</sub> HPs co-existed with well-defined morphologies, and their sizes were preserved without any further ripening, verifying that the synthesis was well-controlled (Fig. 1g). (ii) Besides electrostatic interactions, the huge surface energy of CsPbBr<sub>3</sub> QDs could drive its face-to-face attaching to Co<sub>3</sub>O<sub>4</sub> HPs. (iii) CsPbBr<sub>3</sub> QDs were well dispersed (denoted by yellow circles) all over Co<sub>3</sub>O<sub>4</sub> HPs, both on the inner side (Fig. 1g and inset) and on the boundary sides (Fig. 1h) and this would facilitate the formation of a rich heterointerface. (iv) Even though most of the mesopores were occupied by CsPbBr<sub>3</sub> QDs, still many mesopores could be observed as denoted by the marked area in green (Fig. 1g, h, and the inset).

Such accessible mesopores are not only beneficial for supporting CO<sub>2</sub> adsorption but also facilitate the exposure of the innermost lattice surfaces for the rapid transfer of photo-induced e<sup>-</sup> to the outermost active surface sites.<sup>52,57</sup> More clear evidence regarding the formation of the heterointerface was collected *via* high-resolution TEM analysis (HRTEM, Fig. 1i and j). The spacing in the lattice fringes was found to match well with both constituents, that is, 0.58 nm and 0.285 nm being the corresponding planes of CsPbBr<sub>3</sub> and Co<sub>3</sub>O<sub>4</sub> respectively (Fig. 1j). Accordingly, the HAADF and energy dispersive X-ray (EDX) mapping analysis depicts the precise incorporation and distribution of all elements including Cs, Pb, Br, Co, and O in the CsPbBr<sub>3</sub>-Co<sub>3</sub>O<sub>4</sub> heterojunction (Fig. 1k-p). The above results are in-line with the XRD and TEM analysis, validating the formation of the heterojunction with finely dispersed CsPbBr<sub>3</sub> QDs on the support matrix of Co<sub>3</sub>O<sub>4</sub> HPs.

Next, surface chemical states and interfacial interaction in the CsPbBr<sub>3</sub>-Co<sub>3</sub>O<sub>4</sub> heterojunction were evaluated *via* high-resolution X-ray photoelectron spectroscopy (XPS) of Cs 3d, Pb 4f, Br 3d, Co 2p, and O 1s. It is noteworthy that, in comparison with CsPbBr<sub>3</sub> QDs, the binding energy of Cs 3d (Fig. 2a), Pb 4f



**Scheme 1** Illustration for the formation of the CsPbBr<sub>3</sub>-Co<sub>3</sub>O<sub>4</sub> heterojunction *via* electrostatic attraction.

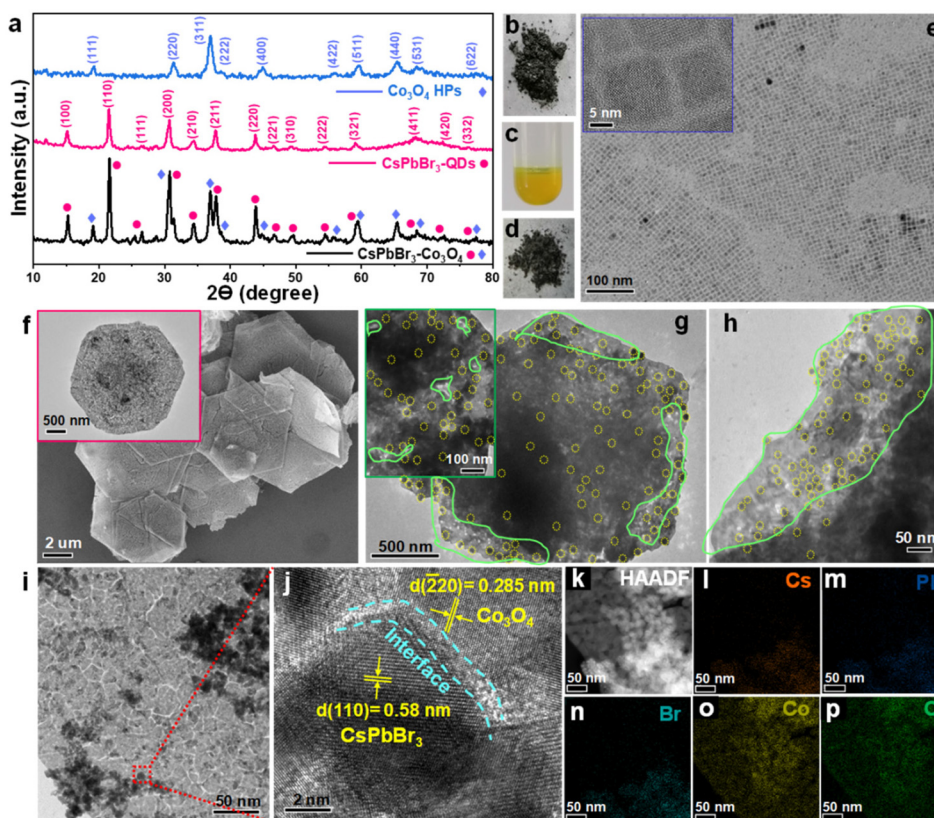


**Fig. 1** (a) Comparison of the XRD pattern for the as-prepared products within the 2 theta range  $10^{\circ}$ – $80^{\circ}$ , where pink circles and blue diamonds denote the corresponding peaks in the  $\text{Co}_3\text{O}_4$ – $\text{CsPbBr}_3$  heterojunction originating from pristine products. Exclusive color transformation of the as-synthesized products where (b)  $\text{Co}_3\text{O}_4$  HPs black, (c)  $\text{CsPbBr}_3$  QDs bright yellow, and (d)  $\text{CsPbBr}_3$ – $\text{Co}_3\text{O}_4$  dark grey. (e) The TEM image of pristine  $\text{CsPbBr}_3$  QDs and the corresponding inset with high magnification. (f) The SEM image with low magnification and the inset is the TEM image for a single particle of  $\text{Co}_3\text{O}_4$  HPs showing a hexagonal platelet-like morphology. (g) The TEM image of a  $\text{Co}_3\text{O}_4$ – $\text{CsPbBr}_3$  heterojunction and the corresponding inset which was captured from the central side of a random particle and (h) the image taken from the boundary side. Finely dispersed  $\text{CsPbBr}_3$  QDs are denoted with yellow circles and the pores are denoted with green marked areas. (i) and (j) HRTEM images, and (k–p) HAADF and EDX mapping results for the  $\text{Co}_3\text{O}_4$ – $\text{CsPbBr}_3$  heterojunction.

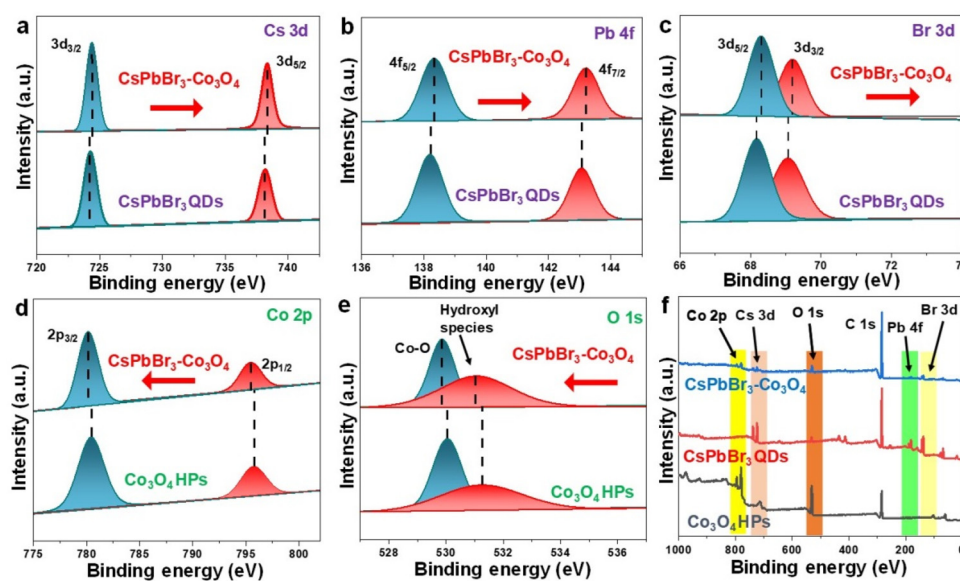


**Fig. 2** Comparative representation of high-resolution XPS spectra for (a) Cs 3d, (b) Pb 4f, (c) Br 3d, (d) Co 2p, and (e) O 1s in all the synthesized products. (f) The XPS survey spectrum highlights the co-existence of  $\text{CsPbBr}_3$  QDs and  $\text{Co}_3\text{O}_4$  HPs in the  $\text{CsPbBr}_3$ – $\text{Co}_3\text{O}_4$  heterojunction.

(Fig. 2b), and Br 3d (Fig. 2c) faced a positive shift in the heterojunction. This result strongly endorsed the close interfacial contact between QDs and HPs. Meanwhile, the XPS of Co 2p spectra signals were comparatively examined for CsPbBr<sub>3</sub>-Co<sub>3</sub>O<sub>4</sub> and Co<sub>3</sub>O<sub>4</sub> HPs (Fig. 2d), where two binding energy values at 796 ± 0.2 eV and 780 ± 0.2 eV fit to Co 2p<sub>1/2</sub> and Co 2p<sub>3/2</sub>, respectively, which normally attributed to two main regions *i.e.*, Co<sup>2+</sup> and Co<sup>3+</sup>.<sup>44</sup> As is known the theoretical value for the atomic ratio Co<sup>2+</sup>/Co<sup>3+</sup> is 0.5 (*i.e.*, perfect Co<sub>3</sub>O<sub>4</sub>), but this value may increase in the presence of surface defects or oxygen vacancies (OVs).<sup>44</sup> Herein, no signal corresponding to defects in O 1s spectra (Fig. 2e) was found, which means that Co<sub>3</sub>O<sub>4</sub> synthesized here is perfect and in an equally balanced state. Notably, the absence of OVs also indicates that the high crystallinity of Co<sub>3</sub>O<sub>4</sub> was maintained after forming the CsPbBr<sub>3</sub>-Co<sub>3</sub>O<sub>4</sub> heterojunction. Meanwhile, a slight negative shift towards the lower binding energy was observed, demonstrating the interaction between Co<sub>3</sub>O<sub>4</sub> and CsPbBr<sub>3</sub> (Fig. 2d). Moreover, relative O 1s spectra disclosed two main peaks that fit with the hydroxyl species and Co-O bond respectively. In addition, the obvious co-existence of CsPbBr<sub>3</sub> QDs and Co<sub>3</sub>O<sub>4</sub> HPs is supported through the XPS survey spectrum (Fig. 2f). All the characteristic peaks are assigned to Cs, Pb, Br, Co, and O (highlighted with bars), affirming the formation of the CsPbBr<sub>3</sub>-Co<sub>3</sub>O<sub>4</sub> heterojunction.

### 3.2. Investigation of the photocatalytic activity for CO<sub>2</sub> reduction

The activity of the as-synthesized CsPbBr<sub>3</sub>-Co<sub>3</sub>O<sub>4</sub> heterojunction for CO<sub>2</sub> photocatalytic reduction is evaluated under the solid-gas environment using 50 μL of water as the proton source (see details in the ESI section 1.3†).<sup>36,38,63</sup> In particular, no sacrificial agent was used, and visible light was irradiated during photocatalysis. As shown in Fig. 3a, the pristine components only can produce limited CO and negligible CH<sub>4</sub>, calculated to be 14.23 and 0.39 (for CsPbBr<sub>3</sub> QDs) and 9.52 and 0.46 (for Co<sub>3</sub>O<sub>4</sub> HPs) μmol g<sup>-1</sup> h<sup>-1</sup>, respectively. Notably, the CsPbBr<sub>3</sub>-Co<sub>3</sub>O<sub>4</sub> heterojunction delivered an enhanced performance for the evolution of CO and CH<sub>4</sub>, which is 35.40 and 29.2 μmol g<sup>-1</sup> h<sup>-1</sup>, respectively. The corresponding electron consumption rate ( $R_{\text{electron}}$ , see the formula in Table S2†) was found to be 304.4 μmol g<sup>-1</sup> h<sup>-1</sup>, which is 9.51 and 13.4 fold larger than that of pristine CsPbBr<sub>3</sub> QDs and Co<sub>3</sub>O<sub>4</sub> HPs,

respectively. The maximum cumulative production of CO and CH<sub>4</sub> after a 6-hour reaction was 211.58 and 175.31 μmol g<sup>-1</sup>, respectively (Fig. S6†). The current performance of the CsPbBr<sub>3</sub>-Co<sub>3</sub>O<sub>4</sub> heterojunction was found to be exceeding that of the pristine counter components as well as recent state-of-the-art photocatalysts (Table S1†). Moreover, altering the dosage ratio of Co<sub>3</sub>O<sub>4</sub>:CsPbBr<sub>3</sub> in the heterojunction could greatly influence the activity, for instance, the upper limit of gases was only reached with an optimum mass ratio of 1:4 (Fig. S7†).

More and/or less dosage of CsPbBr<sub>3</sub> than the optimum value in the heterojunction is not conducive to producing CO and CH<sub>4</sub> in high yields, maybe due to the insufficient amount and/or blockage of active sites respectively, and this phenomenon was found to be consistent with the literature.<sup>38</sup> Additionally, control experiments were performed to confirm the origin of CO, and CH<sub>4</sub> during photocatalysis (Fig. 3b). First, under an argon atmosphere, traces of CO or CH<sub>4</sub> was found, which shows that feed-stock CO<sub>2</sub> is necessary to run the photocatalytic reduction reaction.<sup>36,38,63</sup> Second, nothing was detected under the dark conditions, which again confirms light irradiation is required to obtain CO and CH<sub>4</sub> from the reduction of CO<sub>2</sub>. Finally, the optimum result could only be achieved using the CsPbBr<sub>3</sub>-Co<sub>3</sub>O<sub>4</sub> heterojunction with a mass ratio of 1:4 as the photocatalyst, CO<sub>2</sub> gas as the feedstock, and solar light illumination ( $\lambda > 400$  nm). To further verify the origin of the carbon source of the photo-generated CO and CH<sub>4</sub>, <sup>13</sup>CO<sub>2</sub> isotope labelling was performed and the GC-MS result is displayed in Fig. S8.† Evidently, the signals belonging to <sup>13</sup>CO ( $m/z$  29) and <sup>13</sup>CH<sub>4</sub> ( $m/z$  17) are derived from <sup>13</sup>CO<sub>2</sub>, validating that CO<sub>2</sub> feedstock is the actual carbon source. Likewise, the oxidation of water to oxygen further validates the continuous supply of protons during CO<sub>2</sub> conversion (Fig. S9†). Furthermore, the CsPbBr<sub>3</sub>-Co<sub>3</sub>O<sub>4</sub> heterojunction can remain stable during the consecutive 5 cycles (Fig. 3c). The morphological and structural characteristics of the CsPbBr<sub>3</sub>-Co<sub>3</sub>O<sub>4</sub> heterojunction are well-maintained after photocatalysis (Fig. S10a and S10b†).

### 3.3. Unveiling of the origins for improved activity

The origins of the possible enhanced activity were investigated and have been described systematically. The CO<sub>2</sub> adsorption

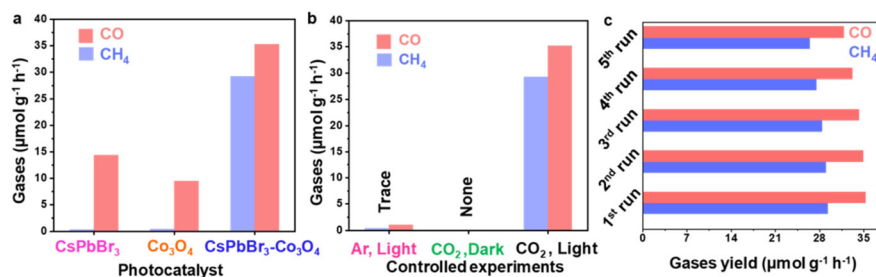


**Fig. 3** (a) A comparative depiction of the catalytic activity in terms of the produced gases CO and CH<sub>4</sub> using the as-synthesized CsPbBr<sub>3</sub> QDs, Co<sub>3</sub>O<sub>4</sub> HPs, and CsPbBr<sub>3</sub>-Co<sub>3</sub>O<sub>4</sub> heterojunction. (b) Controlled experiments were performed under different reaction conditions to produce CO and CH<sub>4</sub> to examine the origin of the evolved gases. (c) Stability test of the CsPbBr<sub>3</sub>-Co<sub>3</sub>O<sub>4</sub> heterojunction for 5 consecutive cycles.

on the surface of the photocatalyst is a primary step that would further govern its activation and conversion. And it is well-known that CsPbBr<sub>3</sub> QDs have a large surface area and are capable of adsorbing more CO<sub>2</sub> on their surface.<sup>32,43</sup> As verified by the TEM analysis, the size of CsPbBr<sub>3</sub> QDs remained unchanged after forming a hybrid with Co<sub>3</sub>O<sub>4</sub> HPs, indicating that it would exhibit similar CO<sub>2</sub> adsorption activity on its surface. Likewise, Co<sub>3</sub>O<sub>4</sub> HPs also possess numerous adsorption sites derived from their structural mesopores. Although most of the mesopores are occupied by CsPbBr<sub>3</sub> QDs (Fig. S11 and Table S2†), additional porosities are still accessible in the heterojunction (as shown in the green marked area in Fig. 1g and h). These porosities would actively endure the CO<sub>2</sub> adsorption.<sup>52,57</sup>

As the light absorption range is a key factor in solar-driven catalysis, to investigate the light-harvesting ability of the as-prepared components, diffuse reflectance spectra (DRS) were recorded. Both CsPbBr<sub>3</sub> QDs and Co<sub>3</sub>O<sub>4</sub> HPs show a strong visible light response within the wavelength range of 400–600 nm, and their corresponding energy band gaps ( $E_g$ ), determined to be 2.36 eV and 2.31 eV, respectively, are well-consistent with the literature (Fig. 4a and b and corresponding insets).<sup>38,52</sup> Where;  $E_g$  is estimated through Tauc plots using the equation  $ah\nu = A(h\nu - E_g)^n$  (see details in section 1.5 of the ESI†). It is to be noted that  $E_{1g} = 1.83$  eV is attributed to the O<sup>2-</sup> → Co<sup>3+</sup> excitation and is not a real energy bandgap of Co<sub>3</sub>O<sub>4</sub> HPs.<sup>52,64–66</sup> The enhanced light absorption ability of both components in the CsPbBr<sub>3</sub>-Co<sub>3</sub>O<sub>4</sub> heterojunction supports its higher catalytic activity. Moreover, the valence and conduction band positions ( $E_{VB}$  and  $E_{CB}$ ) strongly define the thermodynamic feasibility of CO<sub>2</sub> reduction reactions. According to the reported results, the  $E_{CB}$  of Co<sub>3</sub>O<sub>4</sub> and CsPbBr<sub>3</sub> are -0.64 eV<sup>52</sup> and -0.99 eV,<sup>36</sup> respectively, and cor-

respondingly, the calculated  $E_{VB}$  for Co<sub>3</sub>O<sub>4</sub> HPs and CsPbBr<sub>3</sub> QDs are 1.67 eV and 1.37 eV, respectively. Hence, the consequent CsPbBr<sub>3</sub>-Co<sub>3</sub>O<sub>4</sub> heterojunction possess efficient light harvesting ability with staggered band alignment as depicted in Fig. 5a, further endorsing an uninterrupted CO<sub>2</sub> conversion.

The rapid radiative recombination of photoinduced e<sup>-</sup>-h<sup>+</sup> pairs in pristine CsPbBr<sub>3</sub> QDs can lead to low CO<sub>2</sub> conversion efficiency.<sup>24</sup> This was exclusively observed, where the intense photoluminescence (PL) spectra signal for pristine CsPbBr<sub>3</sub> (Fig. 4c) confirmed its low catalytic activity. However, after immobilizing CsPbBr<sub>3</sub> QDs on Co<sub>3</sub>O<sub>4</sub> HPs, the results dramatically changed towards low PL intensity, identifying the significantly hindered recombination of e<sup>-</sup>-h<sup>+</sup> pairs over the CsPbBr<sub>3</sub>-Co<sub>3</sub>O<sub>4</sub> heterojunction (Fig. 4c and Fig. S12†). This finding matched well with the enhanced photocatalytic performance. This also means, combining such photocatalysts can substantially quench the radiative recombination of the metal halide perovskite, thereby exhibiting high activity. Likewise, to investigate the charge transfer kinetics, PL decay was also inquired *via* time-resolved photoluminescence spectroscopy (TRPL, curves were fitted with a bi-exponential function, Table S3† and Fig. 4d). The CsPbBr<sub>3</sub>-Co<sub>3</sub>O<sub>4</sub> heterojunction demonstrated a shorter lifetime ( $\tau_{avg} = 45.04$  ns) in comparison with pristine CsPbBr<sub>3</sub> QDs ( $\tau_{avg} = 47.43$  ns). This outcome further verified the restrained recombination of e<sup>-</sup>-h<sup>+</sup> pairs and their efficient separation in the CsPbBr<sub>3</sub>-Co<sub>3</sub>O<sub>4</sub> hybrid. Besides charge recombination, charge transfer kinetics and their directional transfer are decisive to realize an improved CO<sub>2</sub> conversion.<sup>61,67,68</sup> Therefore, these were investigated for the CsPbBr<sub>3</sub>-Co<sub>3</sub>O<sub>4</sub> heterojunction through electrochemical impedance spectroscopy (EIS) and transient photocurrent responses (TPR). The smallest arc radius was seen for the CsPbBr<sub>3</sub>-Co<sub>3</sub>O<sub>4</sub> heterojunction followed by CsPbBr<sub>3</sub> QDs

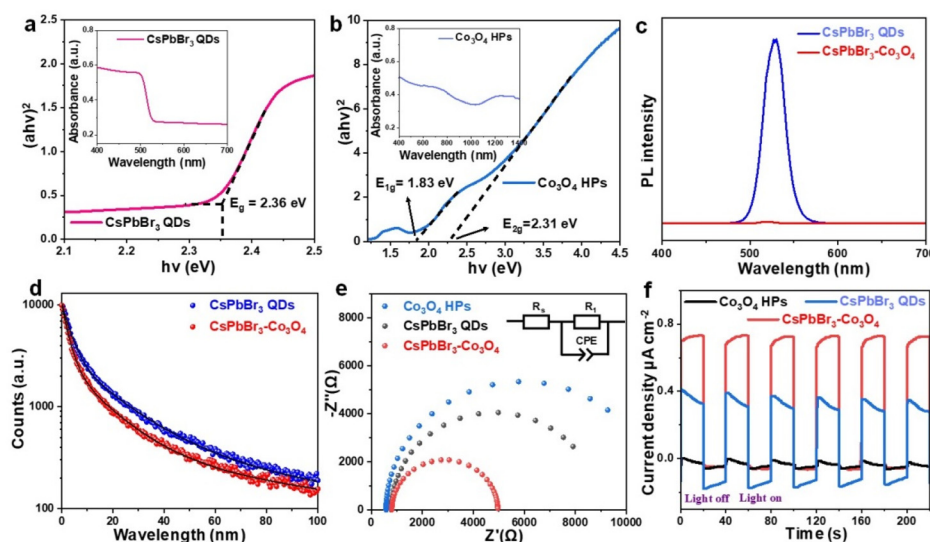


**Fig. 4** Tauc plots for energy bands and their corresponding insets depicting the diffuse reflectance spectra curves for (a) CsPbBr<sub>3</sub> QDs and (b) Co<sub>3</sub>O<sub>4</sub> HPs. (c) Steady-state photoluminescence spectra, and (d) time-resolved photoluminescence spectroscopy of CsPbBr<sub>3</sub> QDs and the CsPbBr<sub>3</sub>-Co<sub>3</sub>O<sub>4</sub> heterojunction. (e) Electrochemical impedance spectra and (f) transient photocurrent spectra of all the as-prepared products.

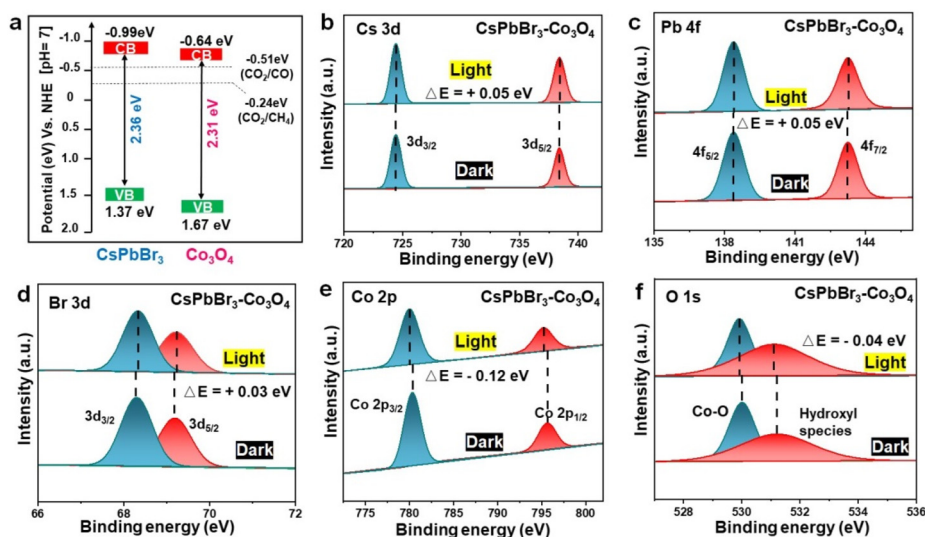


**Fig. 5** (a) Redox potentials and band alignment of the CsPbBr<sub>3</sub>-Co<sub>3</sub>O<sub>4</sub> heterojunction. The *in situ* XPS analysis of (b) Cs 3d, (c) Pb 4f, (d) Br 3d, (e) Co 2p, and (f) O 1s, showing the electron-rich and electron-deficient sides in the CsPbBr<sub>3</sub>-Co<sub>3</sub>O<sub>4</sub> heterojunction.

and Co<sub>3</sub>O<sub>4</sub> HPs (Fig. 4e). The markedly inhibited resistance in CsPbBr<sub>3</sub>-Co<sub>3</sub>O<sub>4</sub> would promote charge transfer. Likewise, the CsPbBr<sub>3</sub>-Co<sub>3</sub>O<sub>4</sub> shows the highest photocurrent with high repeatability (Fig. 4f). This result further supports the accelerated separation of e<sup>-</sup>-h<sup>+</sup> pairs as well as highlights that an accessible route builds up (*i.e.*, heterointerface) by decorating CsPbBr<sub>3</sub> QDs on Co<sub>3</sub>O<sub>4</sub> HPs.

### 3.4. Uncovering charge redistribution on the intimately coupled heterointerface and the corresponding catalytic mechanism

To further shed light on the interfacial charge-carrier flux, and their transfer route, particularly the accumulation of reductive electrons, the *in situ* XPS spectra were conducted under dark and visible light irradiation, respectively. As can be seen, the binding energies corresponding to Cs 3d, Pb 4f, and Br 3d exclusively underwent a positive shift (Fig. 5a-c) under light, which demonstrates a decrease of the electron density in the CsPbBr<sub>3</sub> side. In the meantime, the peak attributed to Co 2p and O 1s shifted to lower binding energy, suggesting an increased electron density at the Co<sub>3</sub>O<sub>4</sub> side (Fig. 5e and f). Such patterns verify the continuous transfer of photoinduced electrons from CsPbBr<sub>3</sub> to Co<sub>3</sub>O<sub>4</sub>. In other words, Co<sub>3</sub>O<sub>4</sub> plays a role as a supporting matrix to evoke and gather electrons from CsPbBr<sub>3</sub> QDs, allowing electron localization on the active surface of Co<sub>3</sub>O<sub>4</sub>. At the same time, an uninterrupted separation of e<sup>-</sup>-h<sup>+</sup> pairs occurs in CsPbBr<sub>3</sub> owing to the significantly improved light harvesting ability and abundant exposed surface. Therefore, the electron-rich and electron-deficient phenomena occur simultaneously to balance the electron redistribution in the CsPbBr<sub>3</sub>-Co<sub>3</sub>O<sub>4</sub> heterojunction. Notably, except for the negative shift in O 1s spectra (Fig. 5f), no new peak belonging to OVs appeared, validating the structural permanence of Co<sub>3</sub>O<sub>4</sub> in the heterojunction.

Furthermore, the work function ( $\Phi$ ) is another pivotal factor for charge carrier kinetics, particularly at the heterointerfaces. The  $\Phi$  for CsPbBr<sub>3</sub> QDs and Co<sub>3</sub>O<sub>4</sub> HPs are 4.39 eV and 5.74 eV respectively.<sup>33,52</sup> So, a larger  $\Phi$  value of Co<sub>3</sub>O<sub>4</sub> refers to its lower Fermi level ( $E_f$ ) than that of CsPbBr<sub>3</sub>, implying that the flow of electrons is from CsPbBr<sub>3</sub> to Co<sub>3</sub>O<sub>4</sub> which is consistent with the outcomes of *in situ* XPS. This would hasten the extraction of reductive electrons from CsPbBr<sub>3</sub> to Co<sub>3</sub>O<sub>4</sub>, thus suppressing the recombination of e<sup>-</sup>-h<sup>+</sup> pairs. In a word, CsPbBr<sub>3</sub> facilitated the rapid and continuous electron transfer *via* shorter diffusion pathways due to the size effect, and Co<sub>3</sub>O<sub>4</sub> spontaneously accepted the electrons and accumulated on its active surface to exclusively participate in CO<sub>2</sub> reduction under the irradiation of solar light.

Based on the above results, the proposed CO<sub>2</sub> photoreduction mechanism over the CsPbBr<sub>3</sub>-Co<sub>3</sub>O<sub>4</sub> hybrid has been described. As illustrated in Fig. 6a, CsPbBr<sub>3</sub> and Co<sub>3</sub>O<sub>4</sub> in the heterojunction have a staggered band alignment (type-II). In addition, the CsPbBr<sub>3</sub>-Co<sub>3</sub>O<sub>4</sub> heterojunction holds enough

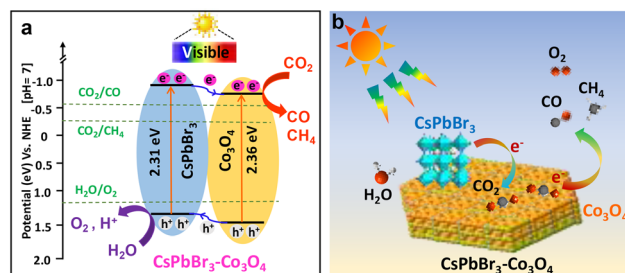


**Fig. 6** (a) Photoexcited charge separation and their transfer route over the CsPbBr<sub>3</sub>-Co<sub>3</sub>O<sub>4</sub> heterojunction under visible light irradiation. (b) Schematic diagram depicting the continuous flow of electrons from CsPbBr<sub>3</sub> towards Co<sub>3</sub>O<sub>4</sub> enabling the photocatalytic conversion of CO<sub>2</sub>.

negative CB and positive VB potentials to reduce CO<sub>2</sub> and oxidize water, respectively. Under light irradiation, electrons and holes can be generated in both CsPbBr<sub>3</sub> and Co<sub>3</sub>O<sub>4</sub>. Subsequently, the photoinduced electrons are transferred from CB of CsPbBr<sub>3</sub> to CB of Co<sub>3</sub>O<sub>4</sub> (Fig. 6b), causing electron localization at the Co<sub>3</sub>O<sub>4</sub> side, making it suitable to conduct the CO<sub>2</sub> reduction reaction (as mentioned earlier in the *in situ* XPS analysis section). In the meantime, holes are transported in opposite directions *i.e.*, from VB of Co<sub>3</sub>O<sub>4</sub> to VB of CsPbBr<sub>3</sub>, building a hole-rich CsPbBr<sub>3</sub> side, favourable for oxidizing H<sub>2</sub>O to O<sub>2</sub> and H<sup>+</sup>. Accordingly, the breaking of C=O bonds in CO<sub>2</sub> occurred at the electron-rich Co<sub>3</sub>O<sub>4</sub> side, where the coupling of electron and protons took place, for instance, 2e<sup>-</sup> and 8e<sup>-</sup> get coupled with 2H<sup>+</sup> and 8H<sup>+</sup> to produce CO and CH<sub>4</sub>, respectively, as presented in eqn (1) and (2). Thus, the effective charge separation enables the uninterrupted electron-proton integrative reaction to realize highly efficient CO<sub>2</sub> photocatalytic reduction over the CsPbBr<sub>3</sub>-Co<sub>3</sub>O<sub>4</sub> heterojunction.



## 4. Conclusions

In conclusion, a facile solution-processed room-temperature method was developed to fabricate a new CsPbBr<sub>3</sub>-Co<sub>3</sub>O<sub>4</sub> heterojunction photocatalyst for visible-light-driven CO<sub>2</sub> conversion. The successful formation of the CsPbBr<sub>3</sub>-Co<sub>3</sub>O<sub>4</sub> hybrid was confirmed by XRD, TEM, HRTEM and XPS analysis. The enhanced generation of CO (35.40 μmol g<sup>-1</sup> h<sup>-1</sup>) and CH<sub>4</sub> (29.2 μmol g<sup>-1</sup> h<sup>-1</sup>) with a high R<sub>electron</sub> rate (304.4 μmol g<sup>-1</sup> h<sup>-1</sup>) was realized on the CsPbBr<sub>3</sub>-Co<sub>3</sub>O<sub>4</sub> hybrid, which outperformed the counter products and some state-of-the-art photocatalysts. The formation of staggered band alignment and an intimately contacted heterointerface led to robust separation and directional transfer of charge carriers. Because of the uninterrupted flow of reductive e<sup>-</sup>, an electron enrichment zone was obtained at the active site of Co<sub>3</sub>O<sub>4</sub>, which ensured the efficient conversion of CO<sub>2</sub>. This work describes the potential of designing a new perovskite-based heterojunction that could enable efficient charge separation to achieve better solar-driven CO<sub>2</sub> conversion.

## Author contributions

Xin Zhong: methodology, investigation, data curation, and writing the original draft. Xinmeng Liang: methodology, investigation, data curation, and writing the original draft. Xinyu Lin: methodology, investigation, and validation. Malik Zeeshan Shahid: writing the original draft, visualization, investigation, and data curation. Jin Wang: supervision, conceptualization, descriptions, and funding acquisition. Zhengquan Li: supervision, conceptualization, descriptions, and funding acquisition.

## Conflicts of interest

There are no conflicts to declare.

## Acknowledgements

This work was financially supported by the National Natural Science Foundation of China (21701143, 21975223), the Natural Science Foundation of Zhejiang Province (LGG19B010002, LZ22B030002), and the Industrial Key Projects of Jinhua City (2021A22383).

## References

- 1 J. Wang, Y. Shi, Y. Wang and Z. Li, Rational design of metal halide perovskite nanocrystals for photocatalytic CO<sub>2</sub> reduction: Recent advances, challenges, and prospects, *ACS Energy Lett.*, 2022, 7, 2043–2059.
- 2 S. Yin, X. Zhao, E. Jiang, Y. Yan, P. Zhou and P. Huo, Boosting water decomposition by sulfur vacancies for efficient CO<sub>2</sub> photoreduction, *Energy Environ. Sci.*, 2022, 15, 1556–1562.
- 3 Y. Feng, C. Wang, P. Cui, C. Li, B. Zhang, L. Gan, S. Zhang, X. Zhang, X. Zhou, Z. Sun, K. Wang, Y. Duan, H. Li, K. Zhou, H. Huang, A. Li, C. Zhuang, L. Wang, Z. Zhang and X. Han, Ultrahigh photocatalytic CO<sub>2</sub> reduction efficiency and selectivity manipulation by single-tungsten-atom oxide at the atomic step of TiO<sub>2</sub>, *Adv. Mater.*, 2022, 34, 2109074.
- 4 J. Wang, L. Xiong, Y. Bai, Z. J. Chen, Q. Zheng, Y. Y. Shi, C. Zhang, G. C. Jiang and Z. Q. Li, Mn-doped perovskite nanocrystals for photocatalytic CO<sub>2</sub> reduction: Insight into the role of the charge carriers with prolonged lifetime, *Sol. RRL*, 2022, 6, 2200294.
- 5 S. Xu, Q. Shen, J. Zheng, Z. Wang, X. Pan, N. Yang and G. Zhao, Advances in biomimetic photoelectrocatalytic reduction of carbon dioxide, *Adv. Sci.*, 2022, 2203941.
- 6 S. H. Teo, C. H. Ng, Y. H. Ng, A. Islam, S. Hayase and Y. H. Taufiq-Yap, Resolve deep-rooted challenges of halide perovskite for sustainable energy development and environmental remediation, *Nano Energy*, 2022, 99, 107401.
- 7 E. Gong, S. Ali, C. B. Hiragond, H. S. Kim, N. S. Powar, D. Kim, H. Kim and S.-I. In, Solar fuels: research and development strategies to accelerate photocatalytic CO<sub>2</sub> conversion into hydrocarbon fuels, *Energy Environ. Sci.*, 2022, 15, 880–937.
- 8 Y. Wang, E. Chen and J. Tang, Insight on reaction pathways of photocatalytic CO<sub>2</sub> conversion, *ACS Catal.*, 2022, 12, 7300–7316.
- 9 Ž. Kovačič, B. Likozar and M. Huš, Photocatalytic CO<sub>2</sub> reduction: A review of Ab initio mechanism, kinetics, and multiscale modeling simulations, *ACS Catal.*, 2020, 10, 14984–15007.

- 10 H. Bian, D. Li, S. Wang, J. Yan and S. F. Liu, 2D-C<sub>3</sub>N<sub>4</sub> encapsulated perovskite nanocrystals for efficient photo-assisted thermocatalytic CO<sub>2</sub> reduction, *Chem. Sci.*, 2022, **13**, 1335–1341.
- 11 S. D. Yang, H. Y. Li, H. M. Li, H. M. Li, W. S. Qi, Q. Zhang, J. Zhu, P. Zhao and L. Chen, Rational design of 3D carbon nitrides assemblies with tunable nano-building blocks for efficient visible-light photocatalytic CO<sub>2</sub> conversion, *Appl. Catal., B*, 2022, **316**, 121612.
- 12 M. Gao, J. Zhang, P. Zhu, X. Liu and Z. Zheng, Unveiling the origin of alkali metal promotion in CO<sub>2</sub> methanation over Ru/ZrO<sub>2</sub>, *Appl. Catal., B*, 2022, **314**, 121476.
- 13 L. Collado, P. Reñones, J. Feroso, F. Fresno, L. Garrido, V. Pérez-Dieste, C. Escudero, M. D. Hernández-Alonso, J. M. Coronado, D. P. Serrano and V. A. D. O'Shea, The role of the surface acidic/basic centers and redox sites on TiO<sub>2</sub> in the photocatalytic CO<sub>2</sub> reduction, *Appl. Catal., B*, 2022, **303**, 120931.
- 14 S. Wei, Q. Heng, Y. Wu, W. Chen, X. Li and W. Shanguan, Improved photocatalytic CO<sub>2</sub> conversion efficiency on Ag loaded porous Ta<sub>2</sub>O<sub>5</sub>, *Appl. Surf. Sci.*, 2021, **563**, 150273.
- 15 X. Lin, S. Xia, L. Zhang, Y. Zhang, S. Sun, Y. Chen, S. Chen, B. Ding, J. Yu and J. Yan, Fabrication of flexible mesoporous black Nb<sub>2</sub>O<sub>5</sub> nanofiber films for visible-light-driven photocatalytic CO<sub>2</sub> Reduction into CH<sub>4</sub>, *Adv. Mater.*, 2022, **34**, 2200756.
- 16 J. Wang, S. Lin, N. Tian, T. Ma, Y. Zhang and H. Huang, Nanostructured metal sulfides: classification, modification strategy, and solar-driven CO<sub>2</sub> reduction application, *Adv. Funct. Mater.*, 2020, **31**, 2008008.
- 17 C. I. Ezugwu, S. Liu, C. Li, S. Zhuiykov, S. Roy and F. Verpoort, Engineering metal-organic frameworks for efficient photocatalytic conversion of CO<sub>2</sub> into solar fuels, *Coord. Chem. Rev.*, 2022, **450**, 214245.
- 18 C. B. Hiragond, N. S. Powar, J. Lee and S. I. In, Single-atom catalysts (SACs) for photocatalytic CO<sub>2</sub> reduction with H<sub>2</sub>O: activity, product selectivity, stability, and surface chemistry, *Small*, 2022, **18**, 2201428.
- 19 X. J. Liu, T. Q. Chen, Y. H. Xue, J. C. Fan, S. L. Shen, M. S. A. A. Hossain, M. A. Amin, L. K. Pan, X. T. Xu and Y. Yamauchi, Nanoarchitectonics of MXene/semiconductor heterojunctions toward artificial photosynthesis via photocatalytic CO<sub>2</sub> reduction, *Coord. Chem. Rev.*, 2022, **459**, 214440.
- 20 S.-H. Wang, F. Khurshid, P.-Z. Chen, Y.-R. Lai, C.-W. Cai, P.-W. Chung, M. Hayashi, R.-J. Jeng, S.-P. Rwei and L. Wang, Solution-processable naphthalene diimide-based conjugated polymers as organocatalysts for photocatalytic CO<sub>2</sub> reaction with extremely stable catalytic activity for over 330 hours, *Chem. Mater.*, 2022, **34**, 4955–4963.
- 21 S. Chen, H. Yin, P. Liu, Y. Wang and H. Zhao, Stabilisation and performance enhancement strategies for halide perovskite photocatalysts, *Adv. Mater.*, 2022, **35**, 2203836.
- 22 H. Huang, D. Verhaeghe, B. Weng, B. Ghosh, H. Zhang, J. Hofkens, J. A. Steele and M. B. J. Roeloffs, Metal halide perovskite based heterojunction photocatalysts, *Angew. Chem., Int. Ed.*, 2022, **61**, e202203261.
- 23 S. Purohit, K. L. Yadav and S. Satapathi, Metal halide perovskite heterojunction for photocatalytic hydrogen generation: progress and future opportunities, *Adv. Mater. Interfaces*, 2022, **9**, 2200058.
- 24 L. Y. Wu, Y. F. Mu, X. X. Guo, W. Zhang, Z. M. Zhang, M. Zhang and T. B. Lu, Encapsulating perovskite quantum dots in iron-based metal-organic frameworks (MOFs) for efficient photocatalytic CO<sub>2</sub> reduction, *Angew. Chem., Int. Ed.*, 2019, **58**, 9491–9495.
- 25 X. Zhu, L. Ge, Y. Wang, M. Li, R. Zhang, M. Xu, Z. Zhao, W. Lv and R. Chen, Recent advances in enhancing and enriching the optical properties of Cl-based CsPbX<sub>3</sub> nanocrystals, *Adv. Opt. Mater.*, 2021, **9**, 2100058.
- 26 M. Ou, W. Tu, S. Yin, W. Xing, S. Wu, H. Wang, S. Wan, Q. Zhong and R. Xu, Amino-assisted anchoring of CsPbBr<sub>3</sub> perovskite quantum dots on porous g-C<sub>3</sub>N<sub>4</sub> for enhanced photocatalytic CO<sub>2</sub> reduction, *Angew. Chem., Int. Ed.*, 2018, **57**, 13570–13574.
- 27 M. Madi, M. Tahir and S. Tasleem, Advances in structural modification of perovskite semiconductors for visible light assisted photocatalytic CO<sub>2</sub> reduction to renewable solar fuels: A review, *J. Environ. Chem. Eng.*, 2021, **9**, 106264.
- 28 Y. F. Mu, W. Zhang, X. X. Guo, G. X. Dong, M. Zhang and T. B. Lu, Water-tolerant lead halide perovskite nanocrystals as efficient photocatalysts for visible-light-driven CO<sub>2</sub> reduction in pure water, *ChemSusChem*, 2019, **12**, 4769–4774.
- 29 L. Clinckemalie, D. Valli, M. B. J. Roeloffs, J. Hofkens, B. Pradhan and E. Debroye, Challenges and opportunities for CsPbBr<sub>3</sub> perovskites in low- and high-energy radiation detection, *ACS Energy Lett.*, 2021, **6**, 1290–1314.
- 30 J. Wang, J. Liu, Z. Du and Z. Li, Recent advances in metal halide perovskite photocatalysts: Properties, synthesis and applications, *J. Energy Chem.*, 2021, **54**, 770–785.
- 31 G. Gao, Q. Xi, H. Zhou, Y. Zhao, C. Wu, L. Wang, P. Guo and J. Xu, Novel inorganic perovskite quantum dots for photocatalysis, *Nanoscale*, 2017, **9**, 12032–12038.
- 32 Q. A. Akkerman, T. P. T. Nguyen, S. C. Boehme, F. Montanarella, D. N. Dirin, P. Wechsler, F. Beiglbock, G. Raino, R. Erni, C. Katan, J. Even and M. V. Kovalenko, Controlling the nucleation and growth kinetics of lead halide perovskite quantum dots, *Science*, 2022, **377**, 1406–1412.
- 33 Z. Zhang, L. Li, Y. Jiang and J. Xu, Step-scheme photocatalyst of CsPbBr<sub>3</sub> quantum dots/BiOBr nanosheets for efficient CO<sub>2</sub> Photoreduction, *Inorg. Chem.*, 2022, **61**, 3351–3360.
- 34 X. Y. Yue, L. Cheng, J. J. Fan and Q. J. Xiang, 2D/2D BiVO<sub>4</sub>/CsPbBr<sub>3</sub> S-scheme heterojunction for photocatalytic CO<sub>2</sub> reduction: Insights into structure regulation and Fermi level modulation, *Appl. Catal., B*, 2022, **304**, 120979.
- 35 C. C. Lin, T. R. Liu, S. R. Lin, K. M. Boopathi, C. H. Chiang, W. Y. Tzeng, W. C. Chien, H. S. Hsu, C. W. Luo, H. Y. Tsai, H. A. Chen, P. C. Kuo, J. Shiue, J. W. Chiou, W. F. Pong,

- C. C. Chen and C. W. Chen, Spin-polarized photocatalytic CO<sub>2</sub> reduction of Mn-Doped perovskite nanoplates, *J. Am. Chem. Soc.*, 2022, **144**, 15718–15726.
- 36 Q. Wang, J. Wang, J. C. Wang, X. Hu, Y. Bai, X. Zhong and Z. Li, Coupling CsPbBr<sub>3</sub> quantum dots with covalent triazine frameworks for visible-light-driven CO<sub>2</sub> reduction, *ChemSusChem*, 2021, **14**, 1131–1139.
- 37 L. Ding, B. Borjigin, Y. Li, X. Yang, X. Wang and H. Li, Assembling an affinal 0D CsPbBr<sub>3</sub>/2D CsPb<sub>2</sub>Br<sub>5</sub> architecture by synchronously in situ growing CsPbBr<sub>3</sub> QDs and CsPb<sub>2</sub>Br<sub>5</sub> nanosheets: enhanced activity and reusability for photocatalytic CO<sub>2</sub> reduction, *ACS Appl. Mater. Interfaces*, 2021, **13**, 51161–51173.
- 38 J. Wang, J. Wang, N. Li, X. Du, J. Ma, C. He and Z. Li, Direct Z-scheme 0D/2D heterojunction of CsPbBr<sub>3</sub> quantum Dots/Bi<sub>2</sub>WO<sub>6</sub> nanosheets for efficient photocatalytic CO<sub>2</sub> reduction, *ACS Appl. Mater. Interfaces*, 2020, **12**, 31477–31485.
- 39 Y. Jiang, H. Y. Chen, J. Y. Li, J. F. Liao, H. H. Zhang, X. D. Wang and D. B. Kuang, Z-Scheme 2D/2D heterojunction of CsPbBr<sub>3</sub>/Bi<sub>2</sub>WO<sub>6</sub> for improved photocatalytic CO<sub>2</sub> reduction, *Adv. Funct. Mater.*, 2020, **30**, 2004293.
- 40 Z. J. Chen, Y. G. Hu, J. Wang, Q. Shen, Y. H. Zhang, C. Ding, Y. Bai, G. C. Jiang, Z. Q. Li and N. Gaponik, Boosting photocatalytic CO<sub>2</sub> reduction on CsPbBr<sub>3</sub> perovskite nanocrystals by immobilizing metal complexes, *Chem. Mater.*, 2020, **32**, 1517–1525.
- 41 S. Wan, M. Ou, Q. Zhong and X. Wang, Perovskite-type CsPbBr<sub>3</sub> quantum dots/UiO-66(NH<sub>2</sub>) nanojunction as efficient visible-light-driven photocatalyst for CO<sub>2</sub> reduction, *Chem. Eng. J.*, 2019, **358**, 1287–1295.
- 42 Z.-C. Kong, J.-F. Liao, Y.-J. Dong, Y.-F. Xu, H.-Y. Chen, D.-B. Kuang and C.-Y. Su, Core@Shell CsPbBr<sub>3</sub>@Zeolitic imidazolate framework nanocomposite for efficient photocatalytic CO<sub>2</sub> reduction, *ACS Energy Lett.*, 2018, **3**, 2656–2662.
- 43 Y. F. Xu, M. Z. Yang, B. X. Chen, X. D. Wang, H. Y. Chen, D. B. Kuang and C. Y. Su, A CsPbBr<sub>3</sub> perovskite quantum dot/Graphene oxide composite for photocatalytic CO<sub>2</sub> reduction, *J. Am. Chem. Soc.*, 2017, **139**, 5660–5663.
- 44 Q. Zhang, P. Yang, H. Zhang, J. Zhao, H. Shi, Y. Huang and H. Yang, Oxygen vacancies in Co<sub>3</sub>O<sub>4</sub> promote CO<sub>2</sub> photoreduction, *Appl. Catal., B*, 2022, **300**, 120729.
- 45 Z. Feng, X. Zhu, J. Yang, K. Zhong, Z. Jiang, Q. Yu, Y. Song, Y. Hua, H. Li and H. Xu, Inherent facet-dominant effect for cobalt oxide nanosheets to enhance photocatalytic CO<sub>2</sub> reduction, *Appl. Surf. Sci.*, 2022, **578**, 151848.
- 46 P. Yang, Q. Zhang, Z. Yi, J. Wang and H. Yang, Rational electronic control of carbon dioxide reduction over cobalt oxide, *J. Catal.*, 2020, **387**, 119–128.
- 47 L. Huang, B. Li, B. Su, Z. Xiong, C. Zhang, Y. Hou, Z. Ding and S. Wang, Fabrication of hierarchical Co<sub>3</sub>O<sub>4</sub>@CdIn<sub>2</sub>S<sub>4</sub> p–n heterojunction photocatalysts for improved CO<sub>2</sub> reduction with visible light, *J. Mater. Chem. A*, 2020, **8**, 7177–7183.
- 48 L. Wang, J. Wan, Y. Zhao, N. Yang and D. Wang, Hollow multi-shelled structures of Co<sub>3</sub>O<sub>4</sub> dodecahedron with unique crystal orientation for enhanced photocatalytic CO<sub>2</sub> reduction, *J. Am. Chem. Soc.*, 2019, **141**, 2238–2241.
- 49 J. Y. Choi, C. K. Lim, B. Park, M. Kim, A. Jamal and H. Song, Surface activation of cobalt oxide nanoparticles for photocatalytic carbon dioxide reduction to methane, *J. Mater. Chem. A*, 2019, **7**, 15068–15072.
- 50 W. Chen, B. Han, C. Tian, X. Liu, S. Liang, H. Deng and Z. Lin, MOFs-derived ultrathin holey Co<sub>3</sub>O<sub>4</sub> nanosheets for enhanced visible light CO<sub>2</sub> reduction, *Appl. Catal., B*, 2019, **244**, 996–1003.
- 51 X. Huang, Q. Shen, J. Liu, N. Yang and G. Zhao, A CO<sub>2</sub> adsorption-enhanced semiconductor/metal-complex hybrid photoelectrocatalytic interface for efficient formate production, *Energy Environ. Sci.*, 2016, **9**, 3161–3171.
- 52 C. Gao, Q. Meng, K. Zhao, H. Yin, D. Wang, J. Guo, S. Zhao, L. Chang, M. He, Q. Li, H. Zhao, X. Huang, Y. Gao and Z. Tang, Co<sub>3</sub>O<sub>4</sub> Hexagonal platelets with controllable facets enabling highly efficient visible-light photocatalytic reduction of CO<sub>2</sub>, *Adv. Mater.*, 2016, **28**, 6485–6490.
- 53 L. Wang, J. Deng, Z. Lou and T. Zhang, Nanoparticles-assembled Co<sub>3</sub>O<sub>4</sub> nanorods p-type nanomaterials: One-pot synthesis and toluene-sensing properties, *Sens. Actuators, B*, 2014, **201**, 1–6.
- 54 L. Li, C. Zhang, R. Zhang, X. Gao, S. He, M. Liu, X. Li and W. Chen, 2D ultrathin Co<sub>3</sub>O<sub>4</sub> nanosheet array deposited on 3D carbon foam for enhanced ethanol gas sensing application, *Sens. Actuators, B*, 2017, **244**, 664–672.
- 55 A. Aljabour, H. Coskun, D. H. Apaydin, F. Ozel, A. W. Hassel, P. Stadler, N. S. Sariciftci and M. Kus, Nanofibrous cobalt oxide for electrocatalysis of CO<sub>2</sub> reduction to carbon monoxide and formate in an acetonitrile-water electrolyte solution, *Appl. Catal., B*, 2018, **229**, 163–170.
- 56 Y. Gu, J. Ding, X. Tong, H. Yao, R. Yang and Q. Zhong, Photothermal catalyzed hydrogenation of carbon dioxide over porous nanosheet Co<sub>3</sub>O<sub>4</sub>, *J. CO<sub>2</sub> Util.*, 2022, **61**, 102003.
- 57 X. Zhu, H. Ji, J. Yi, J. Yang, X. She, P. Ding, L. Li, J. Deng, J. Qian, H. Xu and H. Li, A specifically exposed cobalt oxide/carbon nitride 2D heterostructure for carbon dioxide photoreduction, *Ind. Eng. Chem. Res.*, 2018, **57**, 17394–17400.
- 58 W. Yang, G. Ma, Y. Fu, K. Peng, H. Yang, X. Zhan, W. Yang, L. Wang and H. Hou, Rationally designed Ti<sub>3</sub>C<sub>2</sub> MXene@TiO<sub>2</sub>/CuInS<sub>2</sub> Schottky/S-scheme integrated heterojunction for enhanced photocatalytic hydrogen evolution, *Chem. Eng. J.*, 2022, **429**, 132381.
- 59 X.-T. Liu, B.-H. Li, X.-J. Wang, Y.-L. Li, J. Zhao, Y.-P. Li and F.-T. Li, Enhanced schottky effect in the Ni<sub>2</sub>P cocatalyst via work function up-shift induced by MoO<sub>2</sub> for boosting photocatalytic hydrogen evolution, *ACS Sustainable Chem. Eng.*, 2022, **10**, 10627–10640.
- 60 K. Liu, H. Zhang, T. Fu, L. Wang, R. Tang, Z. Tong and X. Huang, Construction of BiOBr/Ti<sub>3</sub>C<sub>2</sub>/exfoliated montmorillonite Schottky junction: New insights into exfoliated montmorillonite for inducing MXene oxygen functional-

- zation and enhancing photocatalytic activity, *Chem. Eng. J.*, 2022, **438**, 135609.
- 61 Y. Li, Q. Zhao, Y. Zhang, Y. Li, L. Fan, F.-T. Li and X. Li, In-situ construction of sequential heterostructured CoS/CdS/CuS for building “electron-welcome zone” to enhance solar-to-hydrogen conversion, *Appl. Catal., B*, 2022, **300**, 120763.
- 62 J. Li, L. Xu, T. Wang, J. Song, J. Chen, J. Xue, Y. Dong, B. Cai, Q. Shan, B. Han and H. Zeng, 50-Fold EQE Improvement up to 6.27% of solution-processed all-inorganic perovskite CsPbBr<sub>3</sub> QLEDs via surface ligand density control, *Adv. Mater.*, 2017, **29**, 1603885.
- 63 N. Li, X. Chen, J. Wang, X. Liang, L. Ma, X. Jing, D. L. Chen and Z. Li, ZnSe Nanorods-CsSnCl<sub>3</sub> perovskite heterojunction composite for photocatalytic CO<sub>2</sub> reduction, *ACS Nano*, 2022, **16**, 3332–3340.
- 64 D. Barreca, C. Massignan, S. Daolio, M. Fabrizio, C. Piccirillo, L. Armelao and E. Tondello, Composition and microstructure of cobalt oxide thin films obtained from a novel cobalt(II) precursor by chemical vapor deposition, *Chem. Mater.*, 2001, **13**, 588–593.
- 65 Z. Hu, L. Hao, F. Quan and R. Guo, Recent developments of Co<sub>3</sub>O<sub>4</sub>-based materials as catalysts for the oxygen evolution reaction, *Catal. Sci. Technol.*, 2022, **12**, 436–461.
- 66 Y. Xu, F. Zhang, T. Sheng, T. Ye, D. Yi, Y. Yang, S. Liu, X. Wang and J. Yao, Clarifying the controversial catalytic active sites of Co<sub>3</sub>O<sub>4</sub> for the oxygen evolution reaction, *J. Mater. Chem. A*, 2019, **7**, 23191–23198.
- 67 W. He, L. Liu, T. Ma, H. Han, J. Zhu, Y. Liu, Z. Fang, Z. Yang and K. Guo, Controllable morphology CoFe<sub>2</sub>O<sub>4</sub>/g-C<sub>3</sub>N<sub>4</sub> p-n heterojunction photocatalysts with built-in electric field enhance photocatalytic performance, *Appl. Catal., B*, 2022, **306**, 121107.
- 68 S. Bai, J. Jiang, Q. Zhang and Y. Xiong, Steering charge kinetics in photocatalysis: intersection of materials syntheses, characterization techniques and theoretical simulations, *Chem. Soc. Rev.*, 2015, **44**, 2893–2939.